Vacuum 205 (2022) 111392

Contents lists available at ScienceDirect

Vacuum

journal homepage: www.elsevier.com/locate/vacuum

# An ion beam spot size monitor based on a nano-machined Si photodiode probed by means of the ion beam induced charge technique

G. Andrini [c], E. Nieto Hernández [a], G. Provatas [b], M. Brajkovic [b], A. Crnjac [b], S. Ditalia Tchernij [a], J. Forneris [a,*], V. Rigato [d], M. Campostrini [d], Z. Siketic [b], M. Jaksic [b], E. Vittone [a]

[a] Physics Dept., University of Torino, and Istituto Nazionale di Fisica Nucleare Sez. Torino, Torino, Italy
[b] Laboratory for Ion Beam Interactions, Ruđer Bošković Institute, Zagreb, Croatia
[c] Dipartimento di Elettronica e Telecomunicazioni, Politecnico di Torino, and Istituto Nazionale di Fisica Nucleare Sez. Torino, Torino, Italy
[d] Istituto Nazionale di Fisica Nucleare, Laboratori Nazionali di Legnaro, Italy

ARTICLE INFO

*Keywords:*
Charge collection efficiency
Silicon
Ion beam induced charge (IBIC)
Ion microbeam

ABSTRACT

In this work the utilization of the Ion Beam Induced Charge (IBIC) technique is explored to assess the resolution a 2 MeV Li + ion microbeam raster scanning a micrometer-sized FIB-machined hollows in a silicon photodiode. The analysis of the maps crossing the FIB machined structures evidenced a drop in charge collection efficiency across the perimeter of the hollows combined with a significant recovery of the signal amplitude at the center of the microstructures, thus forming a micrometer-sized feature which can be exploited to estimate the resolution of the probing beam. The results were interpreted according to numerical simulations based on the Shockley-Ramo-Gunn as originating from a FIB-induced surface space charge density.

These results offered additional information with respect to what achievable by a confocal photocurrent microscopy analysis of the same device, due to the significantly shorter focal depth of the latter with respect to the probing ion beam.

This study suggests the viability of an effective method to evaluate of the resolution of ion microbeams in processes and experiments, which could be beneficial in emerging fields (deterministic implantation, micro-radiobiology, ion lithography) demanding beam spot sizes below the micrometer scale.

## 1. Introduction

MeV ion beams are an appealing and versatile tool for the modification, functionalization and analysis of solid state materials [1]. The steady improvements in the last decade in the focusing and collimation of ion beams [2–6] offer enticing opportunities towards the functionalization of materials at the nanoscale [7,8] and the controlled introduction of individual dopants for single-defect engineering by means of ion implantation [9,10]. For processes involving the employment of MeV beams with spot sizes approaching the nanometre scale, the availability of tools for the accurate control on the beam size and resolution is crucial. The main techniques commonly adopted by the scientific community, such as STIM (Scanning Transmission Ion Microscopy), RBS (Rutherford back-scattering) and PIXE (Particle Induced X-ray Emission) rely on the imaging of patterned standards, e.g. TEM grids to assess the beam resolution [11–13] or resolution standards fabricated by proton beam writing [14,15]. Such approach has however the disadvantage of requiring a dedicated reference standard (typically different from the sample intended to be processed), a separate measurement system, and ion currents ranging from nA (as for PIXE or RBS) to fractions of fA (as for STIM or other single-ion detection techniques). These requirements might represent a limit to the accuracy of the estimation of the beam size at sub-μm scales nanoscale, and its implementation might turn to be unpractical for automated functionalization processes as well as for experiments requiring high positional accuracy and precision.

While the scientific community has recently started to integrate in the target samples themselves reference structures to be used as resources for single ion detection [16] with position sensitivity [10,17], the development of on-target diagnostic tools offering the assessment of the ion beam resolution is still currently unexplored. In this work the possibility to gain spatial information on the size of an MeV ion micro-beam based on charge collection efficiency (CCE) measurements is explored by means of a dedicated Ion Beam Induced Charge (IBIC)

* Corresponding author.
*E-mail address:* jacopo.forneris@unito.it (J. Forneris).

https://doi.org/10.1016/j.vacuum.2022.111392
Received 1 April 2022; Received in revised form 25 July 2022; Accepted 1 August 2022
Available online 31 August 2022

[18] experiment. With this purpose, a custom Si photodiode expressly nano-machined by means of a keV Focused Ion Beam (FIB) is employed. The ion beam resolution is assessed through the analysis of IBIC maps carried out by a model for charge induction in a microstructured p-n junction.

## 2. Experimental

**Focused ion beam Lithography.** The device under test consisted of a TO-5 packaged S1223 Si PIN photodiode by Hamamatsu [19]. The diode was denoted by an almost constant donor concentration $\sim 7 \cdot 10^{13}$ $cm^{-3}$, as inferred from capacitance-voltage measurements. A 0.6 μm thick p + layer with a maximum acceptor concentration of $2 \cdot 10^{19}$ $cm^{-3}$ was estimated by spreading resistance profiling. A 180 nm dead layer thickness was measured by Angle Resolved IBIC. The borosilicate cover window of the TO-5 packaging was removed and the diode milling was performed by raster scanning the focused ion beam (FIB: 30 keV $Ga^+$, ion current ~10 nA, beam resolution <100 nm) across the diode surface. A cross-shaped structure composed of several individual square hollows was fabricated, together with additional alignment triangles, as shown in the Scanning Electron Microscopy (SEM) image in Fig. 1i. The FIB milling process resulted in the selective removal of ~4 μm of material and in the formation of sharp (within the <100 nm FIB spatial resolution) hollow sidewalls, as evidenced in Fig. 1ii by the SEM image (52° sample tilt) of a (10 × 10) $\mu m^2$ square hollow. No further fabrication steps, including annealing, were adopted after the FIB machining.

Fig. 2 shows the current-voltage characteristic of the diode before and after the FIB milling process, respectively. While the forward current is left unaffected by the micromachining by all practical means, the FIB machining resulted in an increase of the leakage current under reverse bias from ~1 nA to ~200 nA. However, such a value resulted to be sufficiently low to allow for the investigation of the device by the IBIC technique.

**Photocurrent analysis.** The device underwent a preliminary assessment of the nano-machined structures response under photocurrent (PC) characterization. The photocurrent induced by a laser source (445 nm wavelength) was mapped as a function of the position of incidence of the beam. The analysis was carried out using a custom confocal microscopy setup, offering a <100 nm positional accuracy in the sample positioning and a ~1 μm laser spot size upon focusing on the sample surface by means of a 100x, 0.95 N A. air objective. PC maps were acquired at 0V applied bias by recording the total measured current as a function of the position of the impinging light beam held at constant optical power of 2 mW. The current measurement was acquired by a 6487 Keithley picoammeter. A typical PC map over a 100 × 100 $\mu m^2$ scan region (pixel size: 200 × 200 $nm^2$) is shown in Fig. 3i; the corresponding 1-dimensional profile, extracted from the region highlighted in yellow in Fig. 3i is shown in Fig. 3ii.

The map shows a current intensity drop over the FIB-machined hollows (corresponding to the 3 μm and 1 μm sized squares). The drop is to be ascribed to the large numerical aperture of the confocal microscope objective, since the defocusing of the laser beam cone with respect to the focal plane resulted in a spot size of ~24 μm at a depth of 4 μm. Therefore, most of the excitation light is scattered and absorbed by the edges of the square hollows, thus resulting in a homogeneous decrease in the photocurrent intensity in the whole FIB-machined region. The sudden PC drop at the edges of the hollows was exploited to estimate the resolution of the impinging laser beam, which was described by a FWHM equal to (0.8 ± 0.4) μm, i.e. compatible with the assessments previously reported in photoluminescence experiments performed on the same experimental setup [20].

**Ion beam microscopy.** IBIC measurements were carried out at the nuclear microprobe beamline of the Laboratory for Ion Beam Interactions of the Ruder Boskovic Institute [21,22] using a 2 MeV $Li^+$ beam (ion current of the order of fA) focused micro-beam raster-scanned over the sample surface. To obtain micrometer spatial resolution, the ion beam was focused using a combination of fine apertures positioned along the beam path, and magnetic quadrupoles in a triplet configuration.

This probing ion was chosen since its penetration depth in Si (~5 μm range [23]) is comparable with the depth of the FIB-machined hollows. This choice of the ion energy enabled to investigate the complementary volume of the Si photodiode with respect to the hollows. Each incident ion generates a measurable charge pulse, which is amplified and processed by a standard charge sensitive electronic chain, composed by a charge-sensitive preamplifier (AMPTEK A250) and spectroscopy amplifier (ORTEC 570). All the measurements were carried out at room temperature and in dark conditions. The increased leakage current observed in the FIB-machined photodiode did not hinder the measurements, as the CCE spectrum acquired from a pristine region of the device

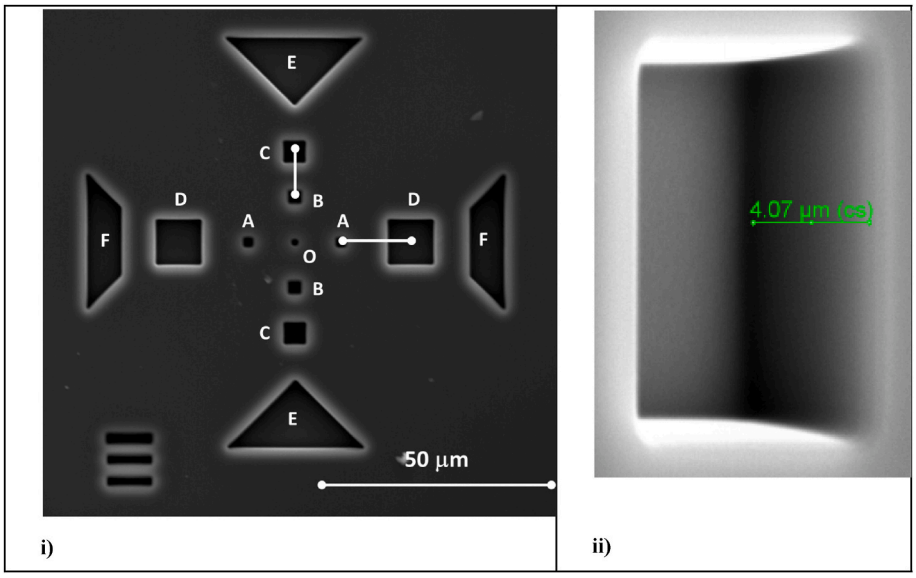


**Fig. 1.** i): SEM image of the diode showing an ordered set of FIB-machined hollows. The nominal sizes of the square edges are 1 μm (O), 2 μm (A), 3 μm (B), 5 μm (C) and 10 μm (D). The distance of the centres of the structures O-A, O–B, B–C is 10 μm; A-D is 15 μm. The distance of the vertices of C-E and of the edges of D-F is 10 μm. i): Cross section of a hollow sidewall (tilt angle: 52°).

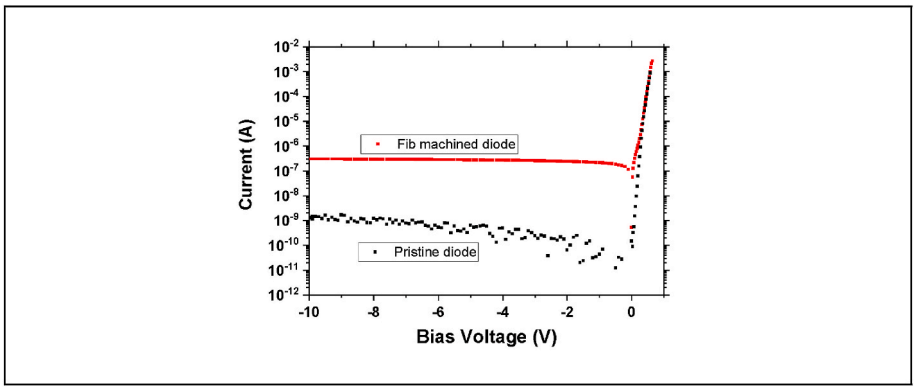


**Fig. 2.** i) Current-voltage characteristic of the pristine and of the FIB machined silicon photodiode.

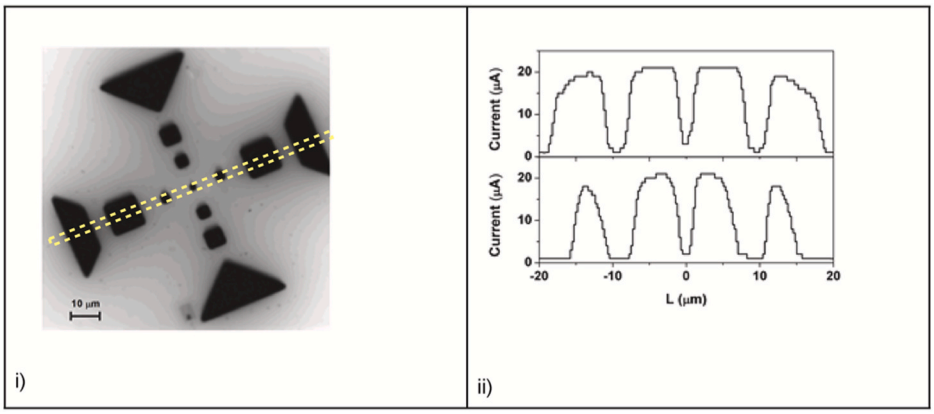


**Fig. 3.** i): Photocurrent map of (200 × 200) $\mu m^2$ acquired from the FIB-machined device using a 2 mW 445 nm laser excitation source under 0 V bias condition. The grayscale encodes the measured photocurrent measured at each pixel of the map. ii): Photocurrent line profiles extracted from Fig. 3i along the two symmetry axes of the FIB-machined device. The abscissa values (L) represent the distance from the central hollow.

in full depletion conditions revealed a 32 keV FWHM. The effective bias voltage across the device was evaluated by subtracting the voltage drop across the 87 MΩ load resistor of the preamplifier from the externally applied bias voltage. The SPECTOR data acquisition system [24] acquires and stores every event along with the coordinates of the ion beam. Induced charge maps are then displayed as the median channel number acquired in each pixel colour or greyscale coded on a map of pixel positions [25].

The ion beam spot size was firstly assessed by Scanning Transmission Ion Microscopy (STIM) of a reference 400 mesh copper grid (Fig. 4i). The 1-dimensional profiles in Fig. 4ii shows the rotation-corrected projection of the region highlighted by the yellow dashed line in Fig. 4i. A regression of the data against error/complementary error functions was performed to quantify the beam spot size as (2.3 ± 0.6) μm, determined

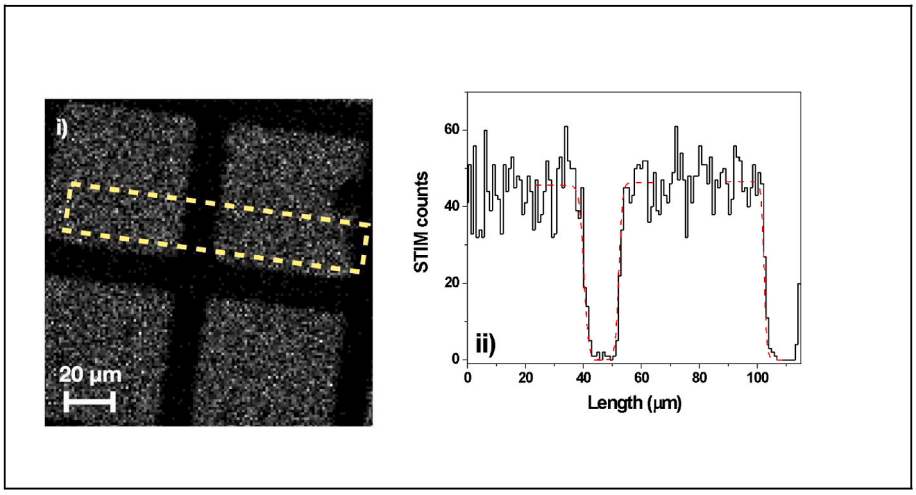


**Fig. 4.** i) STIM map of a 400 mesh acquired using the 2 MeV Li beam. ii) Profile (black line) and corresponding sigmoid fitting curves (red dashed lines) of the STIM counts from the region highlighted in yellow in Fig. 4i.

as the FWHM of the first derivative of the fitting curve.

## 3. Results

**IBIC analysis:** Examples of charge collection efficiency (CCE) maps of the hollow structures at 0 and 2.7 V reverse bias voltage are shown in Fig. 5i) and iii). CCE maps are extracted from IBIC maps by dividing the median channel in each pixel by the peak channel of the IBIC spectrum acquired when the ion beam scans a pristine region in full depletion conditions, i.e. assuming that full collection occurs when e/h pairs are generated in the pristine depletion region.

The CCE maps are encoded in grayscale (top color bar in each figure), which is sufficient to identify the shape of the hollows fabricated on the diode surface. CCE data were extracted from the two orthogonal stripes running along the hollow squares symmetry axes. These lines are highlighted in color in Fig. 5i and **iii)**, where the color scale encodes the CCE value for each individual pixel (0.4 μm and 0.23 μm pixel size for the two maps, respectively). These one-dimensional profiles are quantitatively illustrated in Fig. 5ii) and **iv)**.

It is apparent that the reduction of CCE occurs at the sidewalls of the hollow structures, whereas, quite unexpectedly (and differently with respect to the photocurrent profiles in Fig. 3ii), the CCE significantly recovers its amplitude in the center of the hollows. Additionally, the visibility of the central peak (i.e., the induced charge pulse height at the center of the hollow) seems to be a function both of the applied bias voltage and of the hollow dimensions.

The red curves in Fig. 5iv are the fitting curves of the experimental data, evaluated through a combination of error/complementary error functions to reproduce the data trend at the edge of the hollows and gaussians for the peaks at the centre of the hollows. As for the STIM analysis, the beam spot size was measured through the FWHM of the first derivative of the erf's and erfc's curves, which have a common scaling factor. For the horizontal and vertical profiles, the FWHM are (1.6 ± 0.2) μm and (1.97 ± 0.10) μm, respectively.

## 4. Discussion and numerical analysis

In order to elucidate the causes of this experimental evidence, simulations of induced charge based on the IBIC theoretical model [26,27], have been performed using COMSOL 3.5a software [28].

Briefly, based on the knowledge of the doping profile, previously evaluated by spreading resistance profiling [19], the diode electrostatics was determined by solving the Poisson's and continuity equations, with the boundary conditions normally adopted to simulate semiconductor devices [29,30]: prescribed potential (Dirichlet type conditions) at top and back (grounded) contacts, and insulating (homogeneous Neumann conditions) on the sidewalls of the hollows. In addition, a constant nominal carrier lifetime of the order of tens of μs and conventional expressions of carrier mobilities were assumed [30], which don't account for the effects of the FIB-induced structural stress, on the transport and recombination properties in silicon [33].

Additionally, we assume that the bottom of the hollows can be electrically charged because of the Ga ions implanted during the FIB machining, therefore, the boundary conditions are inhomogeneous Neumann type:

$$(1)\quad -\hat{n}\cdot\vec{D} = \sigma$$

Where $\hat{n}$ is the is the unit outward surface normal vector, $\vec{D}$ is the electric displacement vector and $\sigma$ is the surface charge density. This assumption implies a constant implantation-induced space charge density at the bottom of all the hollows, whose value was assumed as a free parameter for the finite-element simulations. The scheme in Fig. 6 summarizes the adopted boundary conditions relevant to structures C–B–O–B–C shown in Fig. 1. Finally, at the boundaries of the hollows, an infinite recombination velocity is assumed, which is justified by the damage induced by the FIB micromachining.

The Gunn's weighting potential 2D map and the potential contour plot for $\sigma = 0$ and $\sigma = 16$ nC/cm$^2$ are shown in Fig. 7 under 0 V applied electrical bias. It is apparent that beneath the hollows, the Gunn's weighting potential (ψ) is almost null, whereas it is maximum at the top electrode. Therefore, holes generated at the bottom of the hollows contribute to charge induction if they are drifted to the top sensitive electrode, since the induced charge is given by the difference of ψ between the initial and final position of the moving charges [26]. The contribution to the induced charge signals of the minority carriers is then ineffective for $\sigma = 0$ , as the equipotential lines are rather sparse

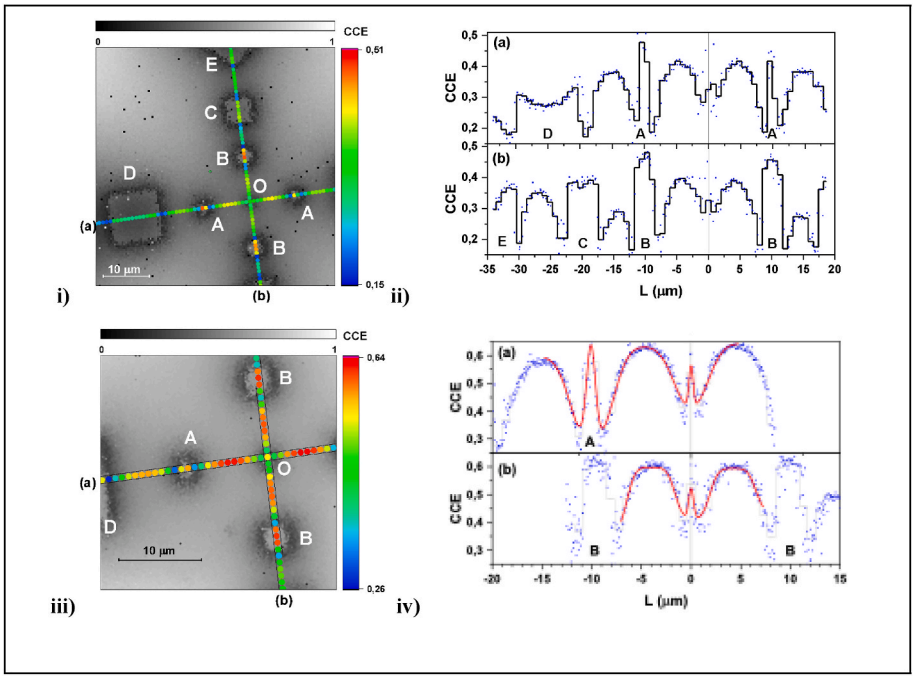


**ig. 5.** i): IBIC map of (47 × 47) μm$^2$ acquired using a 2 MeV Li ion beam from the FIB-machined device under 0 V bias condition; capital letters indicate the structures as in Fig. 1**i**. The top grayscale encodes the median IBIC signal of the pixels in the map. The colour of the markers along the two orthogonal (0.8 μm wide) stripes (a and b) represents the median IBIC signal encoded in the colour scale on the right, whose min and max values are the 1st and 99th percentile of the IBIC signal distribution relevant to pixels in stripes (a) and (b). ii): Median IBIC profiles extracted from the signals of individual pixels (markers) in stripes (a) and (b). The abscissa values (L) represent the distances from the central hollow. iii) (28 × 28) μm$^2$ IBIC map and iv) profiles as in i) and ii), respectively, but for 2.7 V bias voltage. The red curve is the fit of the experimental data by a combination of error and complementary error functions.

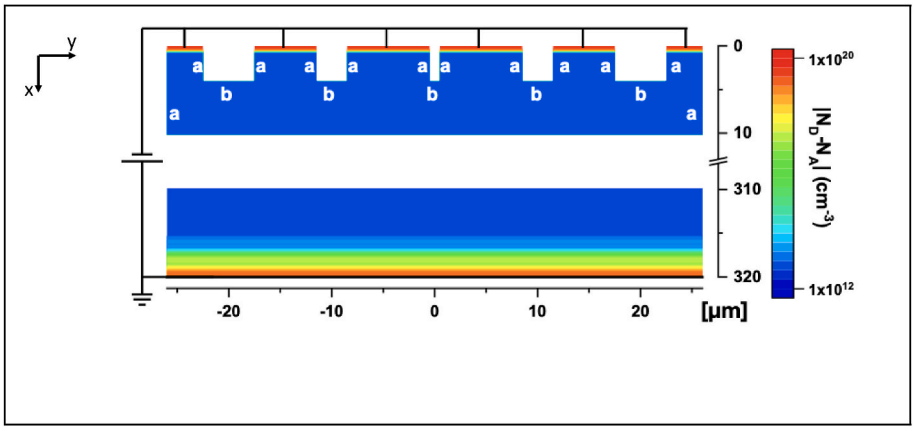


**Fig. 6.** Two dimensional scheme of the diode under study with hollow squares C,B,O,B,C (ref. Fig. 1i)). The surface plot represents the absolute doping concentration encoded in the colour scale on the right ($N_D$ = donor, $N_A$ = acceptor concentrations). The different types of boundaries of the Poisson's equation are identified by "a" (homogeneous Neumann boundary condition), and b (charge surface density, i.e. inhomogeneous Neumann boundary condition) at the bottom of the hollows. The diode is reversed polarized; the bottom electrode is grounded.

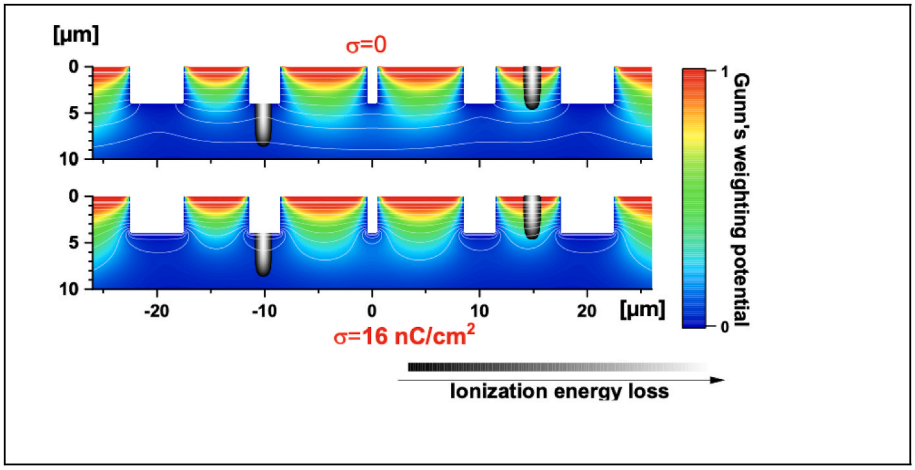


**Fig. 7.** Contour plots of the electrostatic potential at null bias voltage (white contour lines) for $\sigma = 0$ and $\sigma = 16$ nC/cm$^2$ superimposed to the coloured surface maps of the Gunn's weighting potential. The maps refer to the profile including hollow squares C,B,O,B,C (ref. Fig. 1i). The plots encoded in the grayscale represent the ionization energy loss induced by 2 MeV Li ions incident on two different positions: onto the surface (at y = 15) and onto the bottom of the hollow structure B (at y = −10) – see Fig. 1i).

beneath the hollows; however they gather densely, i.e. the electric field strength increases, for $\sigma = 16$ nC/cm$^2$.

Finally, the contributions of electrons ($n^+$) and holes ($p^+$) to the induced charge are calculated by solving the relevant continuity equations in the adjoint form, as described in Refs. [29,31,32].

The results of the two dimensional simulation are given in Fig. 8, where $n^+$, $p^+$ and the total charge collection efficiency (CCE = $n^+$+$p^+$) are mapped in two dimensions for the same structures of Fig. 7, assuming $\sigma = 0$ (left side) and $\sigma = 16\ nC/cm^2$ (right side) at the bottom of the hollows. It is apparent that electron contribution to the induced charge is marginally affected by the surface charge introduced by the Ga ions machining at the bottom of the hollows, whereas holes are efficiently drifted to the top electrode by the electric field induced when $\sigma = 16$ nC/cm$^2$, resulting in a high CCE beneath the hollows.

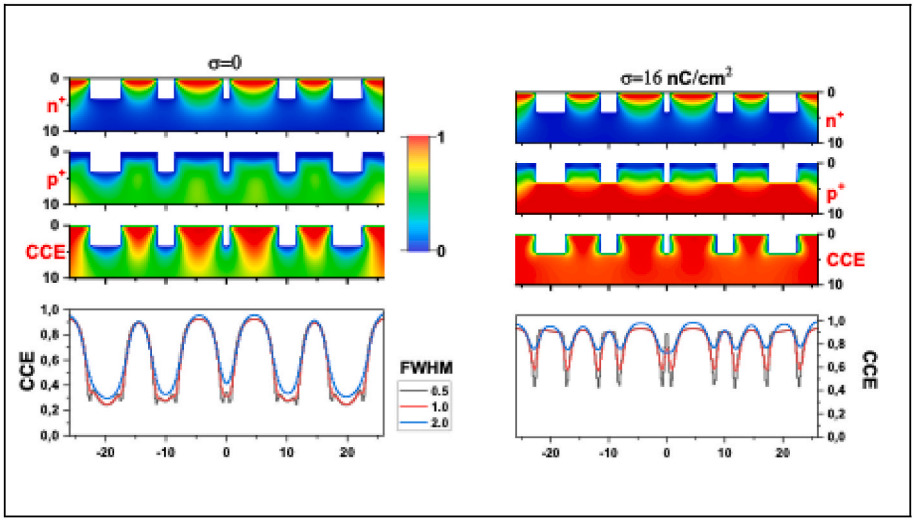


**Fig. 8.** Simulated electrons ($n^+$ - top), holes ($p^+$ - middle) contributions and total (CCE - bottom) charge collection efficiency maps relevant to structures C–B–O–B–C (see Fig. 1) assuming a surface charge at the bottom of the hollows of $\sigma = 0$ (left side) and $\sigma = 16$ nC/cm$^2$ (right side). Bias voltage is null. The graphs at the bottom are the induced charge profiles calculated from the above CCE maps and from the ionization profiles (Fig. 7) calculated for different values of the centroid of the Gaussian beam. The different profiles refer to Gaussians with different FWHM. The dimensional unit is μm for all graphs and maps.

The induced charge profiles have been simulated by the superposition of the contributions of any carrier generated along the trajectory of ions scanning along the y-direction. The electron-hole generation profile Γ of an ion beam incident at the nominal position y = $\xi$, is assumed to be the convolution of the SRIM [21] normalized ionization energy loss profile S(x,y) and the Gaussian profile G(y $\xi$) centred in y = $\xi$:

$$(2)\ \Gamma(x,y;\xi) = \int dy' \cdot \{G(y-y';\xi) \cdot S(x,y')\}$$

Fig. 9 shows the surface map of the electron-hole profile $\Gamma(x,y;\xi=0)$ generated by 2 MeV Li ions at $\xi = 0$ and the relevant projections along the cartesian axes. To give a view of the depth of the Li ion probe with respect to the electrostatic field, the ionization energy loss profiles centred onto the surface and onto the bottom of a hollow are superimposed to the Gunn's weighting potential plot in Fig. 7. It is worth noticing that the shape of $\Gamma(x,y;\xi)$ is assumed to be unaltered both if the ion beam is focused onto the surface or at the bottom of the hollows, due to the large depth of focus of the ion microbeam focusing system, which is typically much larger than depth of the hollows (4 μm) [25].

The induced charge profile P($\xi$) is then calculated for each position $\xi$ of the beam along the surface by integrating over the entire active volume, the generation profile Γ by the charge collection efficiency CCE(x, y):

$$(3)\ P(\xi) = \int dx \int dy \cdot \{CCE(x,y) \cdot \Gamma(x,y;\xi)\}$$

The graphs at the bottom of Fig. 8 show the results of the simulations, assuming a bias voltage of 0 V and Gaussian ion beams with FWHM of 0.5, 1.0, 2.0 μm, for $\sigma = 0$ and $\sigma = 16$ nC/cm$^2$, respectively. In agreement with the above mentioned observations, in the former case the collection of the induced charge when the ion hits the hollow is low, whereas the profiles show peaks at the centre of the hollows in the case of $\sigma = 16\ nC/cm^2$ , which are in qualitative agreement with the experimental profile in Fig. 5, where IBIC peaks emerge at the O,B,C hollows. Furthermore, for the purposes of this study, the comparison of the experimental and simulated profiles appearance of peaks at the central 1 × 1 μm$^2$ hollow leads to conclude that the FWHM of the ion microbeam is smaller than 2 μm.

Fig. 10 shows the simulated induced charge profiles at $V_{bias}$ = 2.7 V

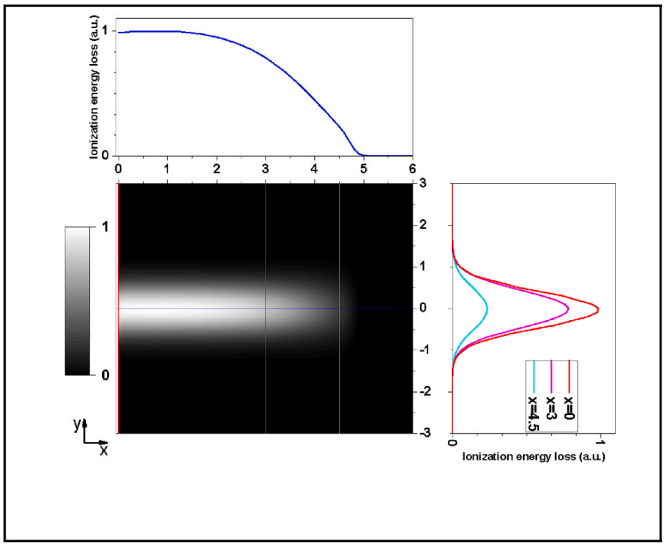


**Fig. 9.** Surface plot and projections along the x and y-axis of the ionization energy loss, assuming a Gaussian beam with FWHM = 1 μm. Dimensional unit are micrometres. The profiles along the y directions are relevant to different depths at x = 0 μm, 3 μm and 4.5 μm.

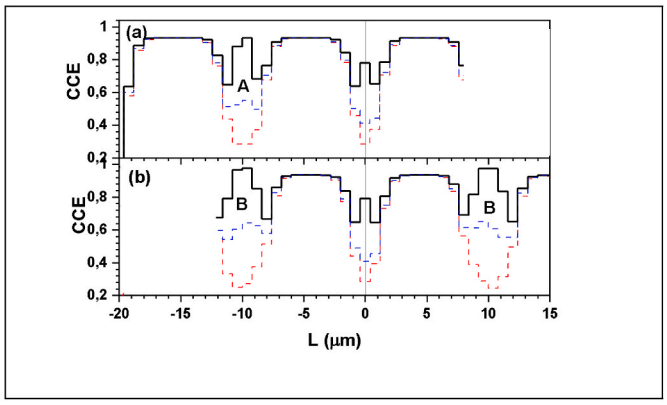


**Fig. 10.** Simulated IBIC profiles as in Fig. 5iv) along the (a) and (b) stripes. Bias voltage = 2.7 V, Gaussian ion beam with FWHM = 1 μm. Dotted red line: σ = 0, Dotted blue line: σ = 1.6 nC/cm$^2$, Continuous black line: σ = 16 nC/cm$^2$. Abscissa represent the distance from the central hollow.

along the (a) and (b) stripes, as in the experimental profiles in Fig. 5iv), assuming a gaussian ion beam with FWHM = 1.0 μm. The simulated profiles qualitatively match the experimental results: the high surface recombination velocity at the hollow sidewalls lowers the IBIC signals, which recovers at the centres of the hollows, as the charge density (σ) increases. It is worth noticing that, as shown in Figs. 7 and 8, even at null bias voltage the surface charge generates an effective electric field permeating the whole region probed by the ions; the widening of the depletion layer at increasing reverse bias voltage do not significantly enhance the motion towards the sensitive electrode of carriers generated beneath the hollows.

## 5. Conclusions

This paper describes IBIC experiments carried out on Si p-n junction diodes with FIB machined hollows at the micrometer scale, using 2 MeV Li microbeams as ion probes.

The FIB microstructures slightly perturb the global electrical characteristics of the diodes, with an acceptably limited increase of the leakage current in reverse polarization, with respect to the pristine samples. The suitability of these hollows to locally modify the functional properties of the diodes was firstly verified through confocal photocurrent microscopy, which provided a clear current intensity drop over the hollows, with a sharp contrast at their edges, which allowed to estimate the laser beam diameter at the focal point.

IBIC maps clearly show a decrease of the signal along the perimeter of the microstructures, whereas in the middle the induced charge recovers to values similar to those generated in pristine regions. The evidence of the CCE drop at the sidewalls, and the apparent peaks observed at the center enabled the evaluation of the beam resolution by adopting the same knife-edge method exploited by the STIM technique. The analysis of the CCE profiles resulted in a beam FWHM estimation, given by (1.6 ± 0.2) μm and (1.97 ± 0.10) μm along the vertical and horizontal profiles, respectively. This result is in line with the discrimination of non-uniform CCE distribution in the inner surface of every hollow, and in particular of the smallest (1 × 1) μm$^2$ structure, which allows to qualitatively set an upper limit to the ion beam dimension of 1–2 μm.

Although compatible, these estimations are lower with respect to what derived from the STIM analysis - which can suffer, in comparison with the proposed IBIC approach, from ion scattering at the edges of the copper grid as well as to its thickness and edge roughness - thus suggesting that the proposed IBIC-based approach could offer a higher accuracy in the estimation of the true value of the ion beam spatial resolution.

The interpretation of such experimental evidence is supported by the well-established IBIC theory, assumption assuming the presence of a

charge density layer implanted during the FIB micro-machining. The presence of such spatial charge density remarkably modifies the electric field beneath the hollows, promoting the drift of minority carriers towards the $p^+$ region and thus enhancing the induced charge at the sensitive electrode. This effect is clearly observed in IBIC maps, resulting from a scanning MeV ion microbeam with a large penetration depth, but is not visible in photocurrent confocal microscopy, where the limited focal depth results in a defocused laser illumination at the bottom preventing the detection of any local enhancement of the photocurrent related to the FIB-induced surface space charge.

The observed results are expected to scale down with the ion beam spot size, the ultimate resolution limit being determined by the lateral straggling of ions in the target substrate [23]. Similarly, the spatial dependence of the CCE is expected to be further enhanced at lower ion energies (e.g. in the keV range of interest in recent deterministic ion implantation experiments [14–16]), for which the surface-related modification of the internal electric field lines would be more pronounced. In this particular case, the application of IBIC methods to nm-thick hollows might have an edge with respect to the range of applicability of techniques, such as PIXE or STIM, relying on the interaction with a μm-thick copper grid standard, where the lack of X-ray production or the sensitivity to elastic scattering with the grid edges would hinder the beam resolution assessment, respectively. The proposed methodology could be exploited as an effective method to estimate the spatial resolution of ion microbeams in experiments or processes, as in deterministic ion implantation, micro-radiodosimetry or micro ion lithography, which require the *in situ* monitoring with high positional accuracy [34–36], thus avoiding the need for a separate reference standard.

## CRediT authorship contribution statement

**G. Andrini:** Writing – review & editing, Writing – original draft, Investigation, Data curation. **E. Nieto Hernández:** Writing – review & editing, Writing – original draft, Investigation. **G. Provatas:** Writing – review & editing, Writing – original draft, Methodology, Investigation, Formal analysis, Data curation. **M. Brajkovic:** Writing – review & editing, Writing – original draft, Validation, Resources, Methodology, Investigation. **A. Crnjac:** Writing – review & editing, Writing – original draft, Validation, Resources, Methodology, Investigation, Data curation. **S. Ditalia Tchernij:** Writing – review & editing, Writing – original draft, Supervision, Resources, Methodology, Investigation, Funding acquisition. **J. Forneris:** Writing – review & editing, Writing – original draft, Supervision, Methodology, Formal analysis, Data curation, Conceptualization. **V. Rigato:** Writing – review & editing, Writing – original draft, Resources, Methodology, Funding acquisition, Conceptualization. **M. Campostrini:** Writing – review & editing, Writing – original draft, Validation, Resources. **Z. Siketic:** Writing – review & editing, Writing – original draft, Supervision, Resources, Project administration, Methodology, Investigation, Funding acquisition. **M. Jaksic:** Writing – review & editing, Writing – original draft, Supervision, Resources, Methodology, Investigation, Conceptualization. **E. Vittone:** Writing – review & editing, Writing – original draft, Visualization, Validation, Supervision, Software, Methodology, Investigation, Formal analysis, Data curation, Conceptualization.

## Declaration of competing interest

The authors declare that they have no known competing financial interests or personal relationships that could have appeared to influence the work reported in this paper.

## Data availability

Data will be made available on request.

## Acknowledgements

This work was supported by the following grants: “Departments of Excellence” (L.232/20165), funded by the Italian Ministry of Education, University and Research (MIUR); “Ex post funding of research - 2020” project of the University of Torino funded by the “Compagnia di San Paolo”; “Training on LASer fabrication and ION implantation of DEFects as quantum emitters” (LasIonDef) project funded by the European Research Council under the “Marie Skłodowska-Curie Innovative Training Networks” program.

The work received the support of the Italian Institute for Nuclear Physics (INFN) within the experiments “ASIDI”, “ROUGE” and “QUANTEP”. J.F. and S.D. gratefully acknowledge the EU H2020 RADIATE Project (proposal 19001744) for granting transnational access to the Laboratories of the Ruđer Bošković Institute.

## References

[1] Y. Yang, Y.G. Li, M.P. Short, C.S. Kim, K.K. Berggren, J. Li, Nano-beam and nano-target effects in ion radiation, Nanoscale 10 (2018) 1598.
[2] F. Watt, M.B.H. Breese, A.A. Bettiol, J.A. van Kan, Proton beam writing, Mater. Today 10 (2007) 20.
[3] A.G. Ponomarev, V.A. Rebrov, S.V. Kolinko, A.S. Lapin, V.F. Salivon, A. A. Ponomarov, The new sumy nuclear microprobe with single-stage quintuplet lens system, Nucl. Instrum. Methods Phys. Res. Sect. B Beam Interact. Mater. Atoms 456 (2019) 21.
[4] Z. Pastuovic, R. Siegele, D.D. Cohen, M. Mann, M. Ionescu, D. Button, S. Long, The new confocal heavy ion microprobe beamline at ANSTO: the first microprobe resolution tests and applications for elemental imaging and analysis, Nucl. Instrum. Methods Phys. Res. Sect. B Beam Interact. Mater. Atoms 404 (2017) 1.
[5] X. Xu, R. Pang, P.S. Raman, R. Mariappan, A. Khursheed, J.A. van Kan, Fabrication and development of high brightness nano-aperture ion source, Microelectron. Eng. 174 (2017) 20.
[6] K.U. Miltenberger, M. Schulte-Borchers, M. Döbeli, A.M. Müller, M. George, H. A. Synal, MeV-SIMS capillary microprobe for molecular imaging, Nucl. Instrum. Methods Phys. Res. Sect. B Beam Interact. Mater. Atoms 412 (2017) 185.
[7] F. Picollo, A. Battiato, L. Boarino, S. Ditalia Tchernij, E. Enrico, J. Forneris, A. Gilardino, M. Jakšić, F. Sardi, N. Skukan, A. Tengattini, P. Olivero, A. Re, E. Vittone, Fabrication of monolithic microfluidic channels in diamond with ion beam lithography, Nucl. Instrum. Methods Phys. Res. Sect. B Beam Interact. Mater. Atoms 404 (2017).
[8] H.D. Liang, Z.Y. Dang, J.F. Wu, J.A. van Kan, S. Qureshi, M.D. Ynsa, V. Torres-Costa, A. Maira, T.V. Venkatesan, M.B.H. Breese, High aspect ratio channels in glass and porous silicon, Nucl. Instrum. Methods Phys. Res. Sect. B Beam Interact. Mater. Atoms 394 (2017) 1.
[9] C. Scheuner, S. Jankuhn, J. Vogt, S. Pezzagna, C. Trautmann, J. Meijer, Nanometer collimation enhancement of ion beams using channeling effects in track-etched mica capillaries, Sci. Rep. 7 (2017) 1.
[10] D.N. Jamieson, W.I.L. Lawrie, S.G. Robson, A.M. Jakob, B.C. Johnson, J. C. McCallum, Deterministic doping, Mater. Sci. Semicond. Process. 62 (2017) 23.
[11] M.J. Simon, M. Döbeli, A.M. Müller, H.A. Synal, In-air STIM with a capillary microprobe, Nucl. Instrum. Methods Phys. Res. Sect. B Beam Interact. Mater. Atoms 273 (2012) 237.
[12] A.D.C. Alves, J. Van Donkelaar, S. Rubanov, P. Reichart, D.N. Jamieson, M. L. Taylor, R.D. Franich, P.N. Johnston, Scanning transmission ion microscopy of nanoscale Apertures, J. Kor. Phys. Soc. 53 (2008) 3704.
[13] J.E. Manuel, S.Z. Szilasi, T.A. Byers, D.Z. Phillips, A.D. Dymnikov, T. Reinert, B. Rout, G.A. Glass, Note: performance of a novel electrostatic quadrupole doublet for nuclear microprobe application, Rev. Sci. Instrum. 89 (2018) 1.
[14] F. Zhang, J.a. van Kan, S.Y. Chiam, F. Watt, Fabrication of free standing resolution standards using proton beam writing, Nucl. Instrum. Methods Phys. Res. Sect. B Beam Interact. Mater. Atoms 260 (2007) 474.
[15] Y. Yao, M.W. Van Mourik, P. Santhana Raman, J.A. Van Kan, Improved beam spot measurements in the 2nd generation proton beam writing system, Nucl. Instrum. Methods Phys. Res. Sect. B Beam Interact. Mater. Atoms 306 (2013) 265.
[16] J.L. Pacheco, M. Singh, D.L. Perry, J.R. Wendt, G. Ten Eyck, R.P. Manginell, T. Pluym, D.R. Luhman, M.P. Lilly, M.S. Carroll, E. Bielejec, Ion implantation for deterministic single atom devices, Rev. Sci. Instrum. 88 (2017).
[17] J. Forneris, V. Grilj, M. Jakšić, P. Olivero, F. Picollo, N. Skukan, C. Verona, G. Verona-Rinati, E. Vittone, Measurement and modelling of anomalous polarity pulses in a multi-electrode diamond detector, EPL (Europhysics Lett. 104 (2013), 28005.
[18] J. Forneris, D.N. Jamieson, G. Giacomini, C. Yang, E. Vittone, Modeling of ion beam induced charge sharing experiments for the design of high resolution position sensitive detectors, Nucl. Instrum. Methods Phys. Res. Sect. B Beam Interact. Mater. Atoms 306 (2013) 169.
[19] Guidelines for Determination of Standardized Semiconductor Radiation Hardness Parameters Being Published on the International Atomic Energy Agency, Technical Report Series, Vienna.

[20] D Gatto Monticone, P. Traina, E. Moreva, J. Forneris, P. Olivero, I.P. Degiovanni, F. Taccetti, L. Giuntini, G. Brida, G. Amato, M. Genovese, Native NIR-emitting single colour centres in CVD diamond, New J. Phys. 16 (2014), 053005.
[21] M. Jakšić, I. Bogdanović Radović, M. Bogovac, V. Desnica, S. Fazinić, M. Karlušić, Z. Medunić, H. Muto, Ž. Pastuović, Z. Siketić, N. Skukan, T. Tadić, New capabilities of the zagreb ion microbeam system, Nucl. Instrum. Methods Phys. Res. Sect. B Beam Interact. Mater. Atoms 260 (2007) 114.
[22] I. Bogdanović Radović, Ruđer Bošković Institute accelerator facility, Nucl. Phys. News 30 (2) (2020) 4–9.
[23] J.F. Ziegler, M.D. Ziegler, J.P. Biersack, SRIM - the stopping and range of ions in matter, Nucl. Instrum. Methods Phys. Res. Sect. B Beam Interact. Mater. Atoms 268 (2010) 1818.
[24] D. Cosic, M. Bogovac, M. Jakšić, Data acquisition and control system for an evolving nuclear microprobe, Nucl. Instrum. Methods Phys. Res. Sect. B Beam Interact. Mater. Atoms 451 (2019) 122.
[25] M.B.H. Breese, D.N. Jamieson, P.J.C. King, Materials Analysis Using a Nuclear Microprobe, John Wiley, New York, 1996.
[26] E. Vittone, Z. Pastuovic, P. Olivero, C. Manfredotti, M. Jaksic, A. Lo Giudice, F. Fizzotti, E. Colombo, Semiconductor characterization by scanning ion beam induced charge (IBIC) microscopy, Nucl. Instrum. Methods Phys. Res. Sect. B Beam Interact. Mater. Atoms 266 (2008) 1312.
[27] G. Vizkelethy, Simulation of ion beam induced current in radiation detectors and microelectronic devices, Nucl. Instrum. Methods Phys. Res. Sect. B Beam Interact. Mater. Atoms 269 (2011) 2330.
[28] COMSOL, Multiphysics Modelling and Simulation, 3.5a.
[29] T.H. Prettyman, Theoretical framework for mapping pulse shapes in semiconductor radiation detectors, Nucl. Instruments Methods Phys. Res. Sect. A Accel. Spectrometers, Detect. Assoc. Equip. 428 (1999) 72.
[30] S. Selberherr, Analysis and Simulation of Semiconductor Devices, Springer-Verlag, Vienna, 1984.
[31] E. Vittone, Z. Pastuovic, P. Olivero, C. Manfredotti, M. Jaksic, A. Lo Giudice, F. Fizzotti, E. Colombo, Semiconductor characterization by scanning ion beam induced charge (IBIC) microscopy, Nucl. Instrum. Methods Phys. Res. Sect. B Beam Interact. Mater. Atoms 266 (2008).
[32] E. Vittone, J. Garcia Lopez, M. Jaksic, M.C. Jimenez Ramos, A. Lohstroh, Z. Pastuovic, S. Rath, R. Siegele, N. Skukan, G. Vizkelethy, A. Simon, Determination of radiation hardness of silicon diodes, Nucl. Instrum. Methods Phys. Res. Sect. B Beam Interact. Mater. Atoms 449 (2019).
[33] V. Moroz, N. Strecker, X. Xu, L. Smith, I. Bork, Modeling the impact of stress on silicon processes and devices, Mater. Sci. Semicond. Process. 6 (2003) 27.
[34] M. Schukraft, J. Zheng, T. Schröder, S.L. Mouradian, M. Walsh, M.E. Trusheim, H. Bakhru, D.R. Englund, Precision nanoimplantation of nitrogen vacancy centers into diamond photonic crystal cavities and waveguides, APL Photonics 1 (2016), 020801.
[35] S. Achilli, H. Le Nguyen, G. Fratesi, N. Manini, G. Onida, M. Turchetti, G. Ferrari, T. Shinada, T. Tanii, E. Prati, Position-controlled functionalization of vacancies in silicon by single-ion implanted germanium atoms, Adv. Funct. Mater. 31 (2021), 2011175.
[36] A. Morello, J.J. Pla, K.W. Chan, K.Y. Tan, H. Huebl, M. Möttönen, C.D. NJugroho, C. Yanh, J.A. Van Donkelaar, A.D.C. Alves, D.N. Jamieson, C.C. Escott, L.C. L. Hollenberg, R.G. Clark, A.S. Dzurak, Single-shot readout of an electron spin in silicon, Nature 467 (2010) 687.